Photoelectron–multiple-photofragment coincidence spectrometer

K. A. Hanold,[a] A. K. Luong, T. G. Clements, and R. E. Continetti[b]
Department of Chemistry and Biochemistry, University of California San Diego, La Jolla, California 92093-0314

(Received 4 December 1998; accepted for publication 29 January 1999)

A new photoelectron–photofragment-coincidence spectrometer is described. Using a multiparticle time- and position-sensitive detector, this apparatus allows the study of dissociation processes of negative ions yielding three photofragments in coincidence with a photoelectron. The photoelectron spectrometer uses two detectors and works in time of flight mode, detecting 10% of the photoelectrons with an energy resolution of 5% at 1.3 eV as shown in studies of the photodetachment of O_2^-. A third detector is used for collection of multiple photofragments (up to 8) in coincidence. This multiparticle detector uses a crossed-delay-line anode and fast timing signals to encode the time- and position-of-arrival of multiple photofragments. The detector was demonstrated to record all three particles produced in a single three-body dissociation event, yielding an energy resolution of $\approx$15% $\Delta E/E$ at 0.7 eV in experiments on the three-body dissociative photodetachment of O_6^-. © *1999 American Institute of Physics.* [S0034-6748(99)02505-8]

I. INTRODUCTION

Although three-body chemical reactions among neutral species play an important role in a number of atmospheric and combustion chemistry systems, the detailed dynamics of these reactions have proven difficult to study. This is primarily due to the need to perform coincidence measurements to determine the correlation between the distribution of internal and kinetic energies among the products. In spite of this, a number of elegant experiments have characterized three-body photodissociation processes by uncorrelated measurements of the momenta and internal energies of one or more of the photofragments.[1–7] Significant insights into both concerted and sequential dissociation reactions have been gained from these experiments. However, a general technique capable of performing the coincidence measurements required us to reveal the partitioning of energy and recoil-angle correlations among the products has not been available for neutral dissociation processes. We have developed a technique for the coincident detection of a photoelectron and multiple neutral photofragments, based on the dissociative photodetachment of molecular and cluster anion precursors. This approach allows a new level of insight into three-body dissociation processes for molecules with a known internal energy.

This new apparatus allows experimental techniques previously used in studies of three-body dissociation processes yielding charged atomic and molecular products to be applied to neutral species. Elegant experiments by Lutz and co-workers on ion-impact-induced Coulomb explosions[8] and by Eland and co-workers[9,10] on dissociative double photoionization have recently achieved complete kinematic measurements of the heavy particle kinetic energy and angular distributions in these processes. Stace and co-workers[11] have also recently carried out an interesting set of experiments in which both positive ion and neutral fragments from the photodissociation of argon cluster ions are detected, providing a detailed view of the correlations between the recoil velocities of an ionic and three neutral products using the covariance mapping technique.[12] An additional level of detail is provided in the kinematically complete photelectron–photoion experiments on the double photoionization of D_2 using the cold target recoil ion momentum spectroscopy pioneered by Schmidt-Bocking and co-workers.[13]

In our experiments, we seek to carry out kinematically complete studies of neutral three-body dissociation reactions at low relative energies. The study of neutral three-body dissociation reactions by dissociative photodetachment of molecular or cluster anion precursors represents an extension of the use of negative-ion photodetachment to carry out transition-state spectroscopy. The seminal experiments in this area relied on interpretation of the photoelectron kinetic energy spectrum to reveal insights into the dynamics on the neutral potential energy surface. Examples of this technique are the studies by Neumark and co-workers of hydrogen exchange reactions[14,15] and by Lineberger and co-workers of isomerization dynamics in small organic molecules.[16,17] We have previously developed experimental techniques to carry out coincidence measurements of the energy and recoil angles of a photoelectron and two photofragments in dissociative photodetachment (DPD) processes.[18] These photoelectron–photofragment coincidence experiments reveal the asymptotic correlation between the dissociation dynamics and the Franck–Condon region accessed by photodetachment. The apparatus described here allows the photoelectron–photofragment coincidence experiment to be carried out on half-collision processes producing three photofragments.

[a]Present address: Syagen Technology, 1411 Warner Ave., Suite B, Tustin, CA 92780.
[b]Electronic mail: rcontinetti@ucsd.edu

Detailed measurements of three-body dissociation processes require a multiparticle detector capable of recording the time- and position-of-arrival of all three particles in coincidence. While measuring two out of three particles suffices to determine momentum conservation if the fragmentation pattern is known, detection of all three particles is necessary to reduce the possibility of false coincidences in the data and to reveal the fragmentation pattern in unknown cases. Dissociation processes at beam energies of several keV typically lead to all fragments arriving at the detector in a range of a few hundred nanoseconds. To avoid bias in the data set it is desirable to minimize any dead time or dead area on the detector face. While false coincidences between the atomic or molecular photofragments can largely be discarded by checking for conservation of momentum, coincidence between the detected photoelectron and the photofragments is determined by the overall detection efficiency for the apparatus. As discussed later, this requires operating the experiment at high-repetition and low-signal rates. These considerations impose significant constraints on the chosen detection scheme. Nonetheless, there are several possible approaches to solving this problem.

While it is beyond the scope of this article to review in detail the approaches that have been taken to detect multiple particles at laboratory energies of several keV,[19] a brief review is in order. For both neutral and charged particles at these energies, it is essential to amplify the signal by production of secondary electrons. Microchannel plates (MCPs) provide the optimum means for doing this over a large detector area (4 cm diam field-of-view), providing gain on the order of 10^7 and detection efficiencies of $\approx$50%. Thus, the question rests on how to encode the time- and position-of-arrival of the electron clouds emerging from the MCP.

In our previous studies, two-body dissociation processes have been studied using an anode split into two side-by-side wedge-and-strip patterned anodes.[20] This works well since the kinematics require that the two bodies for a single breakup appear on opposite sides of the center of mass (CM). An important limitation of this setup is that the detector has a 6-mm-wide dead area that crosses the entire detector in the middle of the 40-mm-diam active area. The anode could be segmented into three pieces, but the increased dead area would severely limit the detectable range of configurations in a three-body breakup.

A ''pixellated'' anode, composed of many discrete detector elements, with dimensions small enough to provide the desired resolution provides an ideal multiparticle anode. Charge-coupled devices (CCDs) or charge-injection devices (CIDs), respectively provide one approach to this limit. In general, however, CCDs and CIDs lack the data throughput rates required in coincidence experiments and do not directly encode the time-of-arrival information for a given particle. Amitay and Zajfman have recently developed a CCD-based device that can detect the time- and position-of-arrival of several particles in coincidence, however, by using alternate means of encoding the time of arrival.[21] The primary limitation of this technique for coincidence experiments of the type reported here is the low data readout rates characteristic of CCDs ($\approx$50 Hz). X-ray astronomy[22] and real-time x-ray diffraction experiments[23] have motivated the development of true time- and position-sensitive pixellated detectors based on application-specific-integrated circuits developed for high-energy particle physics detectors. In these devices, each pixel will be ''fully instrumented,'' capable of recording charge and time information. However, at the desired spatial resolution ($<$100 μm over a 4 cm field-of-view), the number of pixels required and the complexities of circuit development and data acquisition make this an expensive solution at the present time.

An alternate approach involves the use of a number of parallel wires forming a wire plane. Two wire planes that are orthogonal to each other can be used to give information about the two-dimensional positions of the particles impinging on the detector. Position measurement with wire planes has been accomplished by at least three techniques. The charge division technique joins neighboring wires with resistors, and each end of the resistor chain is coupled to charge sensitive electronics.[24] By measuring the fraction of charge at each end of the resistor chain, the position is determined. This technique requires charge integration and is capable of determining the position of only one particle per resistor chain. The second technique couples each wire to a delay line.[25] By measuring the relative time of arrival of the signal at each end of the delay line, the position is determined. Multiple hits in one delay line result in a number of signals from each end of the delay line, however, which may be difficult to disentangle.[26] Both of these techniques have the advantage that a small number of electronics channels are required for the position encoding (two channels per resistor chain or delay line). The third technique of reading out the wire planes is to instrument each wire. A number of Coulomb explosion experiments on small molecules and clusters have used detectors of this type.[27–29] Since the time and charge of the signal on each wire is measured a large number of data acquisition channels are required. This type of detector has the advantage of being able to measure, a large number of particles arriving virtually simultaneously, but often has resolution limited by the spacing of the wires. It should be noted that the wire planes need not be physical wires. For example, in one of the Coulomb explosion experiments, a three-wire-plane anode was fabricated on a single double-sided circuit board by photoetching with interconnects using through-plated holes in the circuit board.[27]

The multiparticle detector we have built is based on the delay-line approach. The anode is composed of four independent quadrants, each composed of a crossed-delay-line anode.[30,31] This represents a compromise with respect to the number of particles detectable from a given event, but maintains high spatial and temporal resolution. With each quadrant instrumented to detect two particles, up to eight photofragments can be recorded for each event. This detector is discussed in more detail in Sec. II B.

In the following sections, the photoelectron-multiple-photofragment coincidence spectrometer is described in detail. In these experiments, photodetachment of a precursor negative ion and energy analysis of the photoelectron is used to prepare a neutral complex with a known internal energy that subsequently dissociates. The photoelectron spectrom-

eter consists of two equivalent detectors on opposite sides of the laser–ion beam interaction region. Each detector is time- and position-sensitive which allows for determination of the photoelectron kinetic energy and recoil angle in the CM frame. Atomic or molecular photofragments recoil out of the fast ion beam, and are measured using the new multiparticle photofragment detector. Following a discussion of the experimental technique, photoelectron and photofragment calibration experiments are presented, along with results on the three-body DPD of O_6^- at 532 nm.

II. EXPERIMENT

Construction of an apparatus capable of detecting, in coincidence, a photoelectron and three photofragments originating from a single dissociation event requires high-efficiency detection schemes. Carrying out photoelectron–photofragment coincidence experiments in a fast ion beam provides a practical route to coincidence detection of multiple photofragments due to the kinematic constraint of all photofragments to a small cone about the ion beam direction. This, coupled with the high detection efficiencies of MCP-based detectors for fast neutrals,[32] allows all the photofragments produced in a dissociation event to be collected with a single detector. Fast neutral beam methods have previously been applied to the study of dissociation dynamics, with fast neutral beams and photofragments produced by charge-exchange[33–35] or photodetachment processes.[20,36] Efficient detection of photoelectrons with high-resolution measurements of photoelectron kinetic energy in a fast beam poses a significant challenge, however, due to the necessity of correcting for the electron-recoil-angle-dependent Doppler shift induced by the fast ion beam.[37] We have previously described a fast-ion beam photoelectron spectrometer,[38] demonstrating that this limitation can be overcome by measuring the energy and recoil angle for each photoelectron. This allowed photoelectron–photofragment coincidence experiments on the DPD of molecular or cluster anions into two photofragments and a free electron to be studied.[39] The apparatus described here has been optimized to increase the detection efficiency of the photoelectrons by a factor of 4 and has a new multiparticle detector allowing measurement of the time- and position-of-arrival of three photofragments in coincidence.

The fast-ion beam apparatus is composed of ion source, acceleration, and time-of-flight regions in addition to the particle detectors comprising the coupled translational energy and photoelectron spectrometers shown in Fig. 1. The ion beam line is similar to that described in Ref. 40. A pulsed molecular beam of pure O_2 operating at 1 kHz is crossed with a 1 keV electron beam, forming O_2^-, O_4^-, O_6^-, and other clusters. After acceleration to 4 keV, a time-of-flight (TOF) mass spectrometer is used to select the anion of interest. The ion beam is defined by two 1 mm apertures (1) spaced 41 cm apart, with the first one at a distance of 192 cm from the ion source. The fast, mass-selected ion beam is intersected with a pulsed laser (~100 ps pulse width Nd:YAG) in an interaction volume ~0.5 mm diameter by 1 mm long (2). Photodetached electrons are measured using

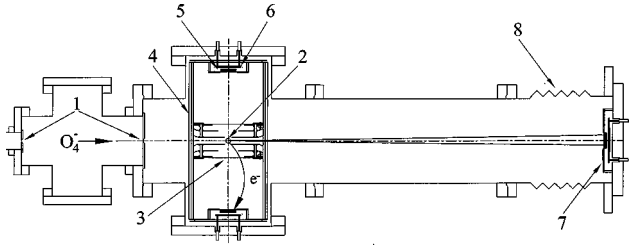

FIG. 1. Schematic diagram (to scale) of the photoelectron–multiple-photofragment spectrometer. The ion beam enters from the left through two 1-mm-diam defining apertures (1). The triple-layer magnetic shield is indicated by (4). The laser is directed out of the page, crossing the ion beam in the interaction region (2). Photoelectrons cross the entrance grid of the electron spectrometer (3) and are accelerated and focused onto the time- and position-sensitive photoelectron detectors (5,6). After exiting the magnetic shields, residual ions are electrostatically removed from the beam and monitored using a microchannel-plate ion detector (not shown). Photofragments recoil out of the beam over a 104 cm flight path and impinge on the multiparticle detector (7). The multiparticle detector is mounted on a bellows (8) so it can be translated in the plane perpendicular to the page.

the photoelectron detectors discussed in detail in Sec. II A. After the ion beam exits the photoelectron spectrometer, residual ions are deflected out of the beam with an electrostatic deflector (not shown), ensuring that only neutral photofragments reach the multiparticle detector (7), described in detail in Sec. II B.

A. Photoelectron detector

The laser–ion beam interaction region is 50 mm from the entrance grid of the two opposed electron detectors. This short flight path dictates that the temporal width of the laser pulse must be less than 0.5 ns for high-resolution TOF spectra and that the laser–ion beam interaction region must be small. Photoelectrons ejected along the axis of the field-free drift regions pass through 81% transmission tungsten grids (3). A triple layer magnetic shield (4, Eagle-AA) encloses the entire electron spectrometer. Electrostatic patch potentials are reduced by practicing standard ultrahigh vacuum techniques and coating exposed surfaces with graphite emulsion. The first element of the detector is an accelerating lens, which focuses the electrons that pass through the 100-mm-diam entrance aperture onto the 40-mm-diam electron detector. In this lens, electrons are accelerated to ~500 V yielding a detection efficiency of about 50%. Three image-quality MCPs (Philips G12-46DT) are used in a *Z*-stack configuration[41] (5) providing a gain of $>10^7$ for detected photoelectrons. The secondary electrons from the MCP stack impinge on a wedge-and-strip-patterned anode (6).[42,43] This anode uses charge division among three conductors to determine the x,y position for a single photoelectron per laser shot. The time of arrival is recorded by using a capacitively coupled 350 MHz amplifier (Ortec VT120) attached to the wedge conductor. The wedge-and-strip anode has been shown under laboratory conditions to be capable of <100 μm local resolution, <500 μm global resolution, and <0.5 ns timing resolution.[38]

Each photoelectron detector accepts electrons ejected into a 110° cone. This large acceptance angle requires correction for both the flight path of each electron and the Dop-

pler correction required to remove the angle-dependent contribution of the ion beam velocity to obtain the CM electron kinetic energy (eKE).[38] The flight path for each electron is geometrically calculated from the measured position of arrival at the detector using the focusing factor of the lens. The laboratory velocity is calculated from this path length and the measured TOF. The field-free flight path of the photoelectrons varies from 50 mm for electrons arriving at the middle of the detector to 85 mm for electrons arriving at the edge of the detector.

The focusing lens was designed using the electrostatic lens simulation program SIMION[44] to be as simple as possible. As shown in Fig. 1, the lens consists of two elements, the ground planes of the inside surface of the magnetic shields (4) and the entrance grid (3), and the 500 V surface of the cylindrical MCP mount (5). Note that the plate behind the MCP mount and the anode (6) is also at ground potential. The radial size of the front plate of the MCP mount determines the focal properties of the lens. This dimension was optimized using SIMION, showing that a one-to-one mapping of electron ejection angle to the measured position-of-arrival for each electron energy is preserved. The lens does, however, exhibit a chromatic aberration in the form of an electron-energy dependent focusing factor, which is approximated by a linear function of the laboratory electron energy. The calculated laboratory position of the photoelectron at the 100-mm-diam entrance grid determines both the flight path and laboratory velocity. The CM velocity is then obtained by vector subtraction of the ion beam velocity from the electron laboratory velocity. Each photoelectron detector subtends approximately twice the solid angle of the fast-ion beam photoelectron detector previously reported.[38] Thus, the photoelectron detection efficiency is a factor of four higher with this new apparatus.

B. Multiparticle detector

The multiparticle detector used in these experiments determines the position of a charge cloud emerging from the MCPs by time division on a delay line.[30,31] This represents a compromise with respect to the number of particles detectable per shot, but maintains high spatial and temporal resolution. In Fig. 2, the layout of the multilayer anode is shown schematically. There are four independent quadrants, each with an active area of 22×22 mm. The serpentine delay lines are positioned outside the field of view. Figure 3 shows a cross section of the multilayer anode, which has four layers and is constructed from a copper-clad ceramic-doped Teflon substrate (RT-Duroid, Rogers Corp.). Layer 1 is a ground plane behind the entire anode. Layer 2 has fingers in one direction while layers 3 and 4 are divided into fingers in the perpendicular direction. The fingers on layers 2 and 4 collect charge for measurement of the x and y positions, and are connected to equally spaced points along two separate serpentine delay lines. The fingers on layer 3 are connected to a ground plane that electronically isolates layers 2 and 4. The charge cloud that hits the anode is large relative to the width of each individual finger (0.47 mm) and is distributed among several neighboring fingers. The signal is then introduced at

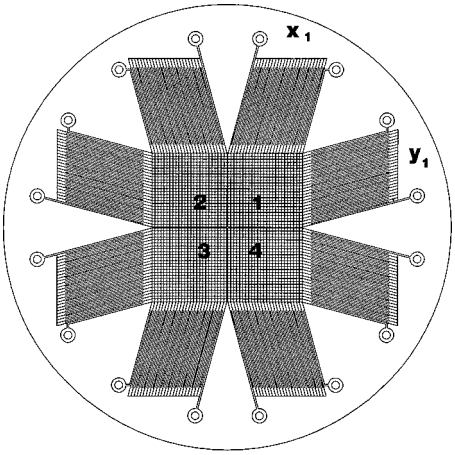

FIG. 2. Schematic layout of the four-quadrant multiparticle anode used in these experiments. Four independent 22×22 mm quadrants composed of crossed charge-collection fingers compose the active area. The x,y delay lines, indicated by x_1,y_1 for quadrant 1, are positioned outside of the field-of-view.

neighboring points along the delay line and propagates to each end, producing pulses of ≈3 ns full width half maximum (FWHM). The time difference between the signals at each end of the delay line is linearly related to position. Using constant-fraction discriminators and a time-to-amplitude converter allows the time difference to be easily measured, using one signal as the start and one as the stop. Given the 20–25 ns propagation time of the signal across the serpentine delay lines, timing resolution on the order of 35 ps is required to achieve the spatial resolution of ≈70 μm.

An advantage of carrying out high-resolution timing on short delay lines is that the dead time for the detector is small. We have taken advantage of this by instrumenting each delay line with a custom-built two-hit time-to-amplitude converter,[45] allowing the measurement of two particles per quadrant. The minimum dead time imposed by the electronics is 7–10 ns. This gives the multiparticle detector the ability to record up to eight photofragments per laser shot in a case of ideal kinematics (two particles per quadrant, with a 10 ns temporal separation). This multiplicity is required to enable detection of three particles arriving in nearly any order and orientation. The charge generated by each event is also measured on each quadrant. Particles whose charge clouds straddle the border of two quadrants are accepted by

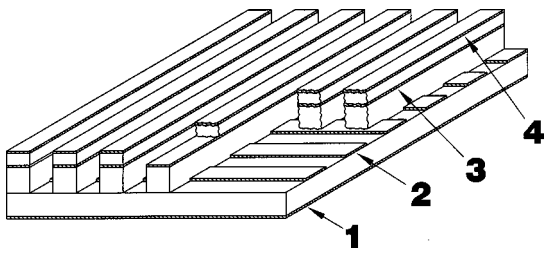

FIG. 3. Schematic view of a cross section of the active area of the multiparticle detector anode. Labels 1, 2, 3, and 4 are photoetched copper layers separated by layers of insulator. Layers 1 and 3 are ground planes. Layers 2 and 4 consist of copper fingers oriented along the x and y axes. These fingers collect and conduct the charge to the serpentine delay line for each coordinate.

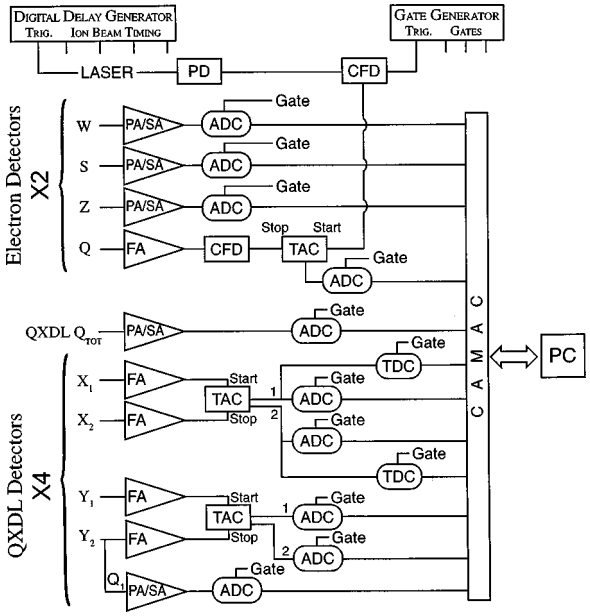

FIG. 4. Schematic diagram of the CAMAC-based data acquisition system. The laser provides the clock for generation of the ion beam and initiation of data collection. The preamplifiers (PA), shaping amplifiers (SA), and fast-timing amplifiers (FA) for one of the photoelectron detectors and one quadrant of the multiparticle (QXDL) detector are shown. The signals from these amplifiers are processed by constant-fraction discriminators (CFDs), time-to-amplitude converters (TACs) and analog-to-digital converters (ADCs) as discussed in the text prior to transfer to a personal computer through the CAMAC interface.

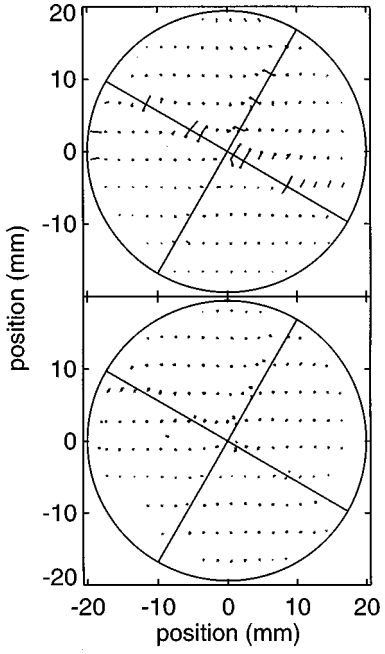

FIG. 5. Pinhole test pattern showing performance of the multiparticle detector. The upper frame shows the raw data with lines that connect the data to the real position of the pinhole. The lower frame shows the data after a numerical correction near the quadrant borders has been applied. The holes are 50 μm in diameter with the exception of the fourth row from the bottom, with 25 μm holes.

electronics for both quadrants. Particles whose time and position of arrival are nearly identical on adjacent quadrants for a given event can be handled by analyzing the charge division between the two quadrants.

C. Data acquisition

The data acquisition system for the experiment is shown in Fig. 4. The central clock for the experiment is the pulsed photodetachment laser, with the previous laser shot providing the start time for production of the pulsed ion beam. The pulsed ion beam switching is controlled by a digital delay generator (SRS DG535). Photoelectron and photofragment data acquisition and timing is initiated by the photodetachment laser pulse as recorded by a fast photodiode triggering one channel of a quad constant fraction discriminator, (CFD, Tennelec TC454). This provides the logic signal for measuring the TOF of the photoelectron and the photofragments and generating the gates required for the single time-to-digital converter (TDC LeCroy 3371) and the four eight-channel analog-to-digital converters (ADC LeCroy 3351) used in data acquisition. Custom-built charge-sensitive preamplifier/shaping amplifier (PA/SA) combinations and fast (300 MHz) timing amplifiers (FA) are used to amplify the signal from the detector anodes.[45] The gates for these ADC and TDC modules are generated by a second SRS DG535 and a home-built gate generator. All the data are transferred to a PC at up to 1 kHz acquisition rates using a computer-automated measurement and control (CAMAC) interface. The multiparticle detector has a total of 16 delay-line signal outputs. These are processed by eight two-hit CFD/time-to-amplitude converter (TAC) modules followed by 16 ADC channels to encode the position-of-arrival of two particles per quadrant. In addition, there are eight TDC channels for recording the time-of-arrival of two particles per quadrant, four ADCs for the charge in each quadrant, and one ADC for the total charge for that event. This is a total of 29 channels. Coupled with the two wedge-and-strip anode photoelectron detectors, each recording three charges and one electron time-of-flight per event, the experiment has 37 data acquisition channels.

The imaging properties and resolution of the multiparticle detector have been determined using a pinhole-pattern resolution mask placed directly on top of the MCPs followed by illumination with ultraviolet photons. The width of the peaks in the resulting image show a local x,y position resolution of $\approx$70 μm. The top frame of Fig. 5 shows the raw image of the pinhole pattern, which consists of rows of holes that are separated by 4 mm with a 2 mm spacing within each row. The fourth row from the bottom has 25-μm-diam holes, while all other rows have 50-μm-diam holes. The borders of the quadrants are shown on Fig. 5, as well as line segments drawn between the actual position of the pinhole in the mask and the detected position of the events from that pinhole. There are a few pinholes that lie on the border of two quadrants and the events from these pinholes appear in both quadrants. The root-mean-square position error away from the quadrant borders is $<$100 μm. A simple power law correction is applied within 3 mm of the quadrant border. The encoded positions in this region are compressed due to charge spilling into the neighboring quadrant, causing the apparent centroid of the charge cloud to be pushed away from the border of the quadrant. The bottom frame of Fig. 5 shows the pinhole pattern after this correction has been ap-

plied. The root-mean-square position error is now <50 μm and is >150 μm for only a few cases near the edge of the field-of-view and the quadrant borders.

D. Coincidence count rates

The acceptable count rate for this experiment is limited by the product of the detection efficiencies for the coincident particles. The multiparticle detector is an essentially zero dead area and a minimum dead time device. The nominal detection efficiency for each of the neutral fragments f_n and the photoelectron f_e is $\approx$50% with an MCP-based detector.[32] If we assume that 100% of the neutral fragments hit the multiparticle detector and 20% of the electron solid angle $\Delta\Omega_e$ is collected with a transmission efficiency T_e of 81%, the average number of true coincidences per laser shot will be

$$n_{\text{true}} = P(1) \cdot f_n^3 f_e \Delta\Omega_e T_e . \tag{1}$$

If we take $P(1)$, the Poisson probability for a single event per shot to be 0.09, Eq. (1) gives a signal count rate of 0.9 Hz when the experiment is run at 1 kHz.

A consideration of sources of background and false coincidences is also important in the design of this experiment. Multiple-event false coincidences can be eliminated by hardware and software charge-discrimination techniques. Conservation of momentum between the atomic or molecular photofragments provides an important means of discarding false coincidences. The most fundamental type of noise in a coincidence experiment of this type, however, is false coincidences between an uncorrelated photoelectron and three correlated photofragments. The rate of these false coincidences is given by

$$n_{\text{False}} = P(2) \cdot 2 \cdot (f_n)^3 \cdot (1 - f_n)^3 \cdot (f_e \Delta\Omega_e T_e) \cdot (1 - f_e \Delta\Omega_e T_e), \tag{2}$$

where $P(2) = 0.016$ is the Poisson probability for two detachment events occurring per laser shot when the average number of events per shot is 0.1. The factor of 2 accounts for the two indistinguishable ways of getting a false coincidence of this type when two DPD events occur. The terms proportional to f_n take into account the probability for detecting three correlated fragments out of the six fragments produced in two dissociative events. Likewise, the terms proportional to f_e relate to the probability of detecting only one out of the two photoelectrons. This gives a false coincidence count rate of 0.04 Hz when the experiment is run at 1 kHz. This is $\approx$4% of the true coincidence count rate and will be negligible for most purposes.

III. RESULTS

A. Photoelectron spectra

The operating characteristics of the photoelectron spectrometer were experimentally verified by photodetachment of a 4 keV beam of O_2^-. Figure 6, frame A, shows the electron laboratory kinetic energy spectrum for photoelectrons that recoil perpendicular to the ion beam direction in the laboratory frame. For these electrons, Doppler broadening from the large ion beam velocity is not significant. There is, however, a noted shift of the laboratory energies to a lower value, relative to the combs on frame C, due to the fact that the correction for the ion beam velocity has not been made to yield the CM eKE in this plot. Clearly defined peaks are visible in this frame. Frame B shows the eKE spectrum for an identical width gate on electron detector positions parallel to the ion beam direction and perpendicular to the laser beam. The Doppler broadening present in these data washes out the structure in the photoelectron spectrum so that only one broad feature is seen. Frame C shows the final eKE spectrum obtained for O_2^- at 532 nm for all electrons independent of position. Determination of this spectrum involves removal of both Doppler broadening and the distribution of field-free flight paths for the photoelectrons in the large-solid-angle photoelectron detectors. Two combs show the expected positions of the photoelectron peaks for photodetachment of $O_2^-(^2\Pi_g) + h\nu \rightarrow O_2(^3\Sigma_g^-), O_2(^1\Delta_g) + e^-$ at 532 nm.[46] Examination of the peak widths shows the energy resolution $\Delta E/E \approx 5\%$ at eKE=1.3 eV.

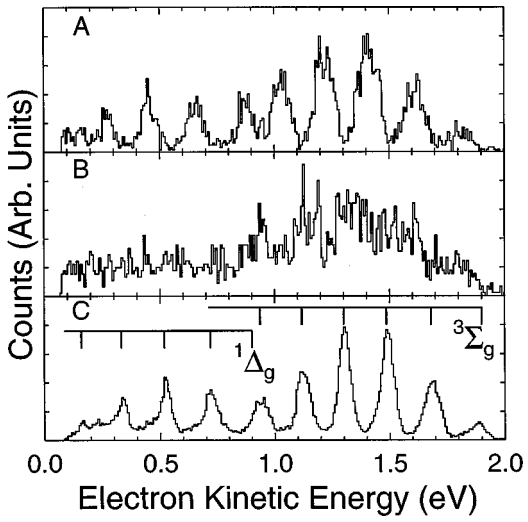

FIG. 6. Photoelectron spectra of O_2^- at 532 nm. Frame A shows the kinetic energy spectrum for electrons recoiling perpendicular to the beam. In frame B, the spectrum for photoelectrons that have velocity components parallel to the beam is shown. Finally, in frame C, the CM photoelectron spectrum after Doppler correction is shown.

B. Three-body photofragment translational spectra

To evaluate the performance of the multiparticle detector for carrying out photofragment translational spectroscopy measurements, initial experiments on the photodissociation and dissociative photodetachment of O_4^- and O_6^- at 532 nm were performed. The photoelectron–photofragment kinetic energy correlations observed in the three-body dissociative photodetachment of O_6^- at 532 nm have been previously reported.[47]

As discussed by DeBruijn and Los,[33] it is straightforward to determine the mass, kinetic energy, and recoil angles of the two photofragments produced in a binary dissociation using a time- and position-sensitive detection scheme. The equations for calculating these quantities from the experimental observables will not be duplicated here.[20,33] Knowing

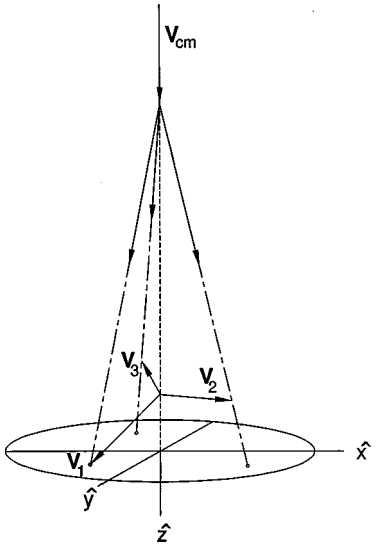

FIG. 7. Kinematic diagram showing a three-body dissociation and the detected position of particle impact on the detector. The incident beam velocity is the velocity of the CM, V_{CM}, and the CM recoil velocities of the three photofragments are shown as V_1, V_2, and V_3.

the parent particle mass and velocity and measuring the time and position-of-impact of two coincident photofragments, it is straightforward to determine the CM translational energy release, recoil angles, and relative masses of the photofragments.

In the case of three-body dissociation, where all the photofragments are recorded in coincidence as in the present experiment, a similar analysis can be carried out. Gardner, Graff, and Kohl discussed fast-beam three-body dissociation experiments and presented equations for determining the photofragment mass from the two-dimensional projection of the CM velocities onto a photofragment detector.[36] In the present experiment, the three-dimensional recoil velocities are recorded. This makes the kinematic analysis of a three-body dissociation in terms of linear momentum conservation in the CM frame straightforward. Figure 7 illustrates the process of a three-body dissociation originating in the interaction region, the subsequent paths of travel of each particle, and the final projection of the three-dimensional event onto the time- and position-sensitive detector. In the analysis of the data, the positions of the particles in the laboratory frame at the time of arrival of the first particle on the detector are calculated using the known velocity of the CM and the flight-time differences of the detected particles.

Each three-body dissociation process is checked for conservation of linear momentum. A CM reference frame using the largest particle velocity vector as the positive z axis is adopted, as shown in Fig. 8. Rotation of the three recoil vectors into this frame allows conservation of momentum and mass to be easily applied to calculate the mass of the three photofragments. The principles of conservation of mass and momentum in the CM frame [Eq. (3)] are then applied to determine the photofragment masses

$$m_1+m_2+m_3=\mathrm{M}, \quad \mathbf{p}_1+\mathbf{p}_2+\mathbf{p}_3=0. \tag{3}$$

The variables m_i are the masses of the three photofragments, M is the parent mass, and $\mathbf{p}_i$ are the photofragment momenta

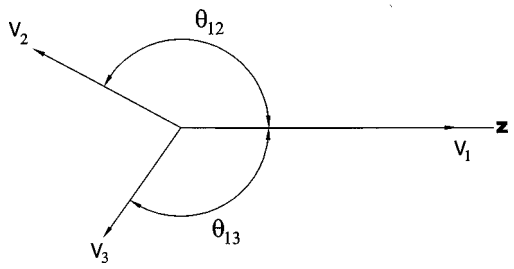

FIG. 8. Kinematic diagram of the CM frame chosen for three-body dissociation processes. The longest CM velocity vector V_1 is chosen as the positive z axis. The polar angles between this velocity vector and the other two fragments in the plane of the breakup are shown as θ_{12} and θ_{13}.

in the CM frame. The momentum of each particle can be decomposed into components along each of the Cartesian axes, and a system of three equations in the three unknowns m_1, m_2, and m_3 can be solved to yield, for example,

$$m_3=\mathrm{M}\left(\frac{\mathrm{V}_{1z}\mathrm{V}_{2y}}{\mathrm{V}_{3y}\mathrm{V}_{2z}-\mathrm{V}_{3z}\mathrm{V}_{2y}-\mathrm{V}_{3y}\mathrm{V}_{1z}+\mathrm{V}_{1z}\mathrm{V}_{2y}}\right). \tag{4}$$

The masses of the other particles can then be determined. The mass spectrum of O_6^- obtained from this technique is shown in Fig. 9, and shows a nominal mass resolution $m/\Delta m \approx 2.5$. In the dissociation of O_6^-, two fragments are fast and one is slow, barely recoiling out of the beam. This limits the mass resolution, since it is based on the recoil distance of the particles relative to the distribution of CM vectors. Fortunately, in the DPD of O_6^- at 532 nm, energetic considerations dictate that three O_2 molecules are produced. Significant improvements in the photofragment mass resolution will require reducing the distribution of velocities of the CM or, in other words, the size of the ion beam at the multiparticle detector. This may be achieved in the future using appropriate collimating ion optics.

Given the photofragment masses and CM velocities, the translational energy released in the three-body dissociation can be calculated by simply adding up the contributions from each particle

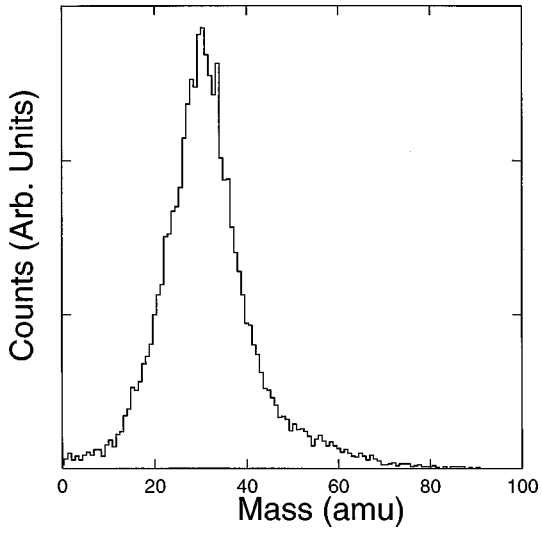

FIG. 9. Photofragment mass distribution recorded for the dissociative photodetachment of O_6^- at 532 nm. The FWHM of the peak is ≈13 amu.

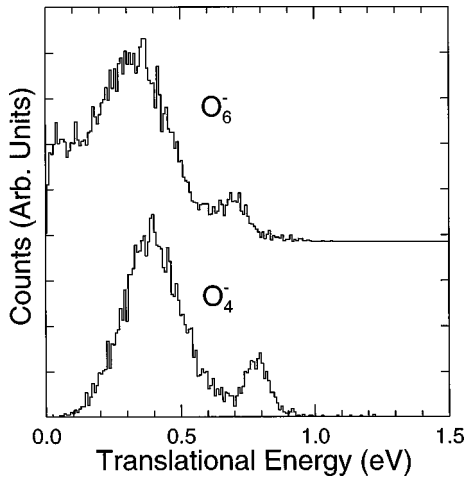

FIG. 10. Photofragment translational energy distributions for the molecular photofragments produced in the dissociative photodetachment of O_4^- and O_6^- at 532 nm.

$$E_T = \tfrac{1}{2}m_1V_1^2 + \tfrac{1}{2}m_2V_2^2 + \tfrac{1}{2}m_3V_3^2. \quad (5)$$

An illustration of the translational energy distributions measured with this detector for both two- and three-body dissociation processes is shown in Fig. 10. This shows translational energy distributions for both O_4^- and O_6^- recorded at 532 nm. The broad feature at 0.4 eV for O_4^- and 0.35 eV for O_6^- is due to the two- and three-body dissociative photodetachment processes in these two species leading to a free electron and separated O_2 molecules. The narrow peaks at 0.8 eV for O_4^- and 0.7 eV for O_6^- result from the photodissociation processes $O_4^- + h\nu \rightarrow O_2(^1\Delta_g) + O_2^-(^2\Pi_g, v=0)$ and $O_6^- + h\nu \rightarrow O_2(^1\Delta_g) + O_2^-(^2\Pi_g, v=0) + O_2(^3\Sigma_g^-)$, respectively. These processes are observable with the negatively biased multiparticle detector due to photodetachment of some of the nascent O_2^- by a second photon. Examination of the width of the feature at 0.7 eV in the O_6^- spectrum indicates an energy resolution $\Delta E/E \approx 15\%$ at 0.7 eV.

The product angular distributions can also provide important insights into the dissociation mechanism. For the dissociative photodetachment of O_6^-, an analysis of the TOF or kinetic energy distributions for each particle in a given event shows that in general there are two fast and one slow O_2 produced. Thus, it appears that this dissociation is nearly a two-body dissociation between two O_2 molecules with the third playing the role of a spectator. Following Fig. 8, the CM recoil angles between the photofragments can be simply calculated from the vectors. In Fig. 11, the angular distributions of the photofragments in the CM frame of the largest recoil velocity are shown. These are generated from raw binned angular distributions by weighting each bin by $1/\sin\theta$. As shown in Fig. 11, the second fastest particle in the CM frame peaks sharply in the opposite direction of the fastest particle, constituting a pseudo two-body dissociation. The third ''spectator'' particle, while also distributed beyond $\theta = \pi/2$ in the CM frame, is seen to have a much broader angular distribution. Given that the fastest particle was assumed to lie along the z axis, and that all three particles have the same mass, this is a consequence of momentum conservation. A detailed analysis of these angular distributions,

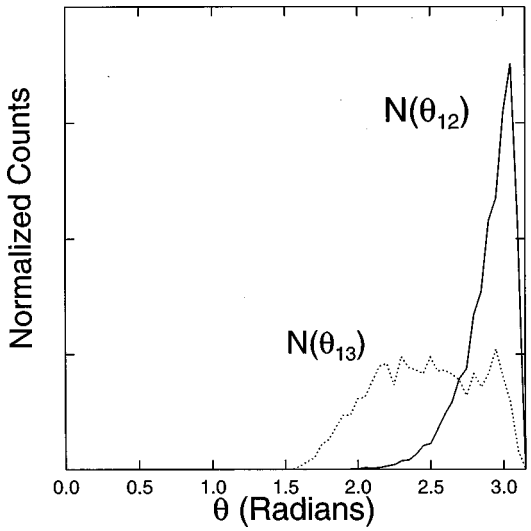

FIG. 11. Photofragment angular distributions for the two slower particles in the CM frame of the fastest particle recoil velocity. These distributions are obtained from the raw histogrammed data by weighting each bin by $1/\sin\theta$ and are normalized to an area of unity. The solid curve, $N(\theta_{12})$, corresponds to the angular distribution of the intermediate velocity particle. The dotted curve, $N(\theta_{13})$, corresponds to the angular distribution of the slowest particle.

perhaps in terms of a classical trajectory simulation, may provide some insights into not only the dissociation dynamics of O_6, but perhaps even the structure of O_6.

There is considerably more detail to be obtained in the study of three-body dissociation dynamics. In a recent comprehensive review article, Maul and Gericke define two primary three-body dissociation mechanisms: concerted and sequential processes.[1] Further classifications of concerted processes into the subcategories of synchronous and asynchronous concerted reactions, according to whether or not multiple bond-breaking processes occur simultaneously, can also be made. These distinctions are not made in the simple data analysis we have carried out to date. In the case when the breakup is sequential, a more complex treatment is needed to fully describe the kinematics of the three-body dissociation process.[48] As more systems are studied, the sensitivity of the data to the various dissociation mechanisms will be assessed with the help of Monte Carlo simulations.

As shown by experiments on the DPD of O_6^-, this apparatus allows studies of the dynamics of three-body dissociation processes induced by photodetachment of stable molecular and cluster anion precursors. Photodetachment, coupled with coincident detection of the photoelectron kinetic energy, provides a novel route to production of neutral molecules or clusters with a known internal energy. Dissociation of these energy-selected species into three photofragments can then be studied using a multiparticle time- and position-sensitive detector described above. In the future, examination of photoelectron–photofragment and photofragment–photofragment angular correlations should provide a direct measure of the time scale for three-body dissociation processes. The next system we hope to extend these measurements to is the three-body association reaction responsible for the formation of ozone: $O + O_2 + M \rightarrow O_3 + M$. The insights into three-body dynamics of neutral molecules and

clusters gained from these experiments should provide an important test of the theories of three-body chemical reactions that are currently being developed.[49]

ACKNOWLEDGMENTS

This work was supported by the Air Force Office of Scientific Research under Grant No. F49620-96-1-0220 and DURIP Grant No. F49620-97-1-0255. One of the authors (A.K.L.) is supported by AFOSR AASERT Grant No. F49620-97-1-0387. R.E.C. is a Camille Dreyfus Teacher-Scholar, an Alfred P. Sloan Research Fellow, and a Packard Fellow in Science and Engineering. The authors thank Dr. O.H.W. Siegmund, R. Raffanti, and J. Hull of Siegmund Scientific Inc. for assistance with the manufacture of the anode and design and assembly of the amplifiers and double-hit time-to-amplitude converters for the multiparticle detector. The contributions of Jacqueline Kessler to construction of circuitry used in the ion beam apparatus are also gratefully acknowledged.

[1] C. Maul and K. H. Gericke, Int. Rev. Phys. Chem. **16**, 1 (1997).
[2] P. M. Kroger and S. J. Riley, J. Chem. Phys. **67**, 4483 (1977).
[3] X. Zhao, W. B. Miller, E. J. Hintsa, and Y. T. Lee, J. Chem. Phys. **90**, 5527 (1989).
[4] C. E. M. Strauss and P. L. Houston, J. Phys. Chem. **94**, 8751 (1990).
[5] T. Gejo, J. A. Harrison, and J. R. Huber, J. Phys. Chem. **100**, 13941 (1996).
[6] S. W. North, A. J. Marr, A. Furland, and G. E. Hall, J. Phys. Chem. A **101**, 9224 (1997).
[7] D. Stranges, X. Yang, J. D. Chesko, and A. G. Suits, J. Chem. Phys. **102**, 6067 (1995).
[8] U. Werner, K. Beckord, J. Becker, and H. O. Lutz, Phys. Rev. Lett. **74**, 1962 (1995).
[9] J. H. D. Eland, *VUV Photoionization and Photodissociation of Molecules and Clusters*, edited by C. Y. Ng (World Scientific, Singapore, 1991), pp. 297–343.
[10] S. Hsieh and J. H. D. Eland, J. Phys. B **30**, 4515 (1997).
[11] P. Jukes, A. Buxey, A. B. Jones, and A. J. Stace, J. Chem. Phys. **14**, 5803 (1998).
[12] L. J. Frasinski, K. Codling, and P. A. Hatherly, Science **240**, 1029 (1989).
[13] R. Dörner *et al.*, Phys. Rev. Lett. **81**, 5776 (1998).
[14] R. B. Metz, S. E. Bradforth, and D. M. Neumark, Adv. Chem. Phys. **81**, 1 (1992).
[15] S. E. Bradforth, D. W. Arnold, D. M. Neumark, and D. E. Manolopoulos, J. Chem. Phys. **99**, 6345 (1993).
[16] K. M. Ervin, J. Ho, and W. C. Lineberger, J. Chem. Phys. **91**, 5974 (1989).
[17] P. G. Wenthold, D. A. Hrovat, W. T. Borden, and W. C. Lineberger, Science **272**, 1456 (1996).
[18] R. E. Continetti, Int. Rev. Phys. Chem. **17**, 227 (1998).
[19] J.-C. Brenot and M. Durup-Ferguson, Adv. Chem. Phys. **82**, 309 (1992).
[20] R. E. Continetti, D. R. Cyr, D. L. Osborn, D. J. Leahy, and D. M. Neumark, J. Chem. Phys. **99**, 2616 (1993).
[21] Z. Amitay and D. Zajfman, Rev. Sci. Instrum. **68**, 1387 (1997).
[22] J. G. Timothy, Opt. Eng. (Bellingham) **24**, 1066 (1985).
[23] P. Datte *et al.*, Nucl. Instrum. Methods Phys. Res. A **391**, 471 (1997).
[24] G. Knapp, Rev. Sci. Instrum. **49**, 982 (1978).
[25] M. B. Williams and S. E. Sobottka, IEEE Trans. Nucl. Sci. **36**, 227 (1989).
[26] J. H. D. Eland and A. H. Pearson, Meas. Sci. Technol. **1**, 36 (1990).
[27] A. Belkacem, A. Faibis, E. P. Kanter, W. Koenig, R. E. Mitchell, Z. Vager, and B. J. Zabransky, Rev. Sci. Instrum. **61**, 945 (1990).
[28] W. Koenig, A. Faibis, E. P. Kanter, Z. Vager, and B. J. Zabransky, Nucl. Instrum. Methods Phys. Res. B **10/11**, 259 (1985).
[29] J. Becker, K. Beckord, U. Werner, and H. O. Lutz, Nucl. Instrum. Methods Phys. Res. A **337**, 409 (1994).
[30] M. Lampton, O. Siegmund, and R. Raffanti, Rev. Sci. Instrum. **58**, 2298 (1987).
[31] P. G. Friedman, R. A. Cuza, J. R. Fleischman, C. Martin, D. Schiminovich, and D. J. Doyle, Rev. Sci. Instrum. **67**, 596 (1996).
[32] A. Müller, N. Djuric', G. H. Dunn, and D. S. Belic', Rev. Sci. Instrum. **57**, 349 (1986).
[33] D. P. DeBruijn and J. Los, Rev. Sci. Instrum. **53**, 1020 (1982).
[34] W. J. van der Zande, W. Koot, J. R. Peterson, and J. Los, Chem. Phys. **126**, 169 (1988); J. H. M. Beijersbergen, S. Kornig, W. J. van der Zande, P. G. Kistemaker, and J. Los, J. Phys. Chem. **95**, 9059 (1991).
[35] H. Helm and P. C. Cosby, J. Chem. Phys. **86**, 6813 (1987).
[36] L. D. Gardner, M. M. Graff, and J. L. Kohl, Rev. Sci. Instrum. **57**, 177 (1986).
[37] H. Hotop and W. C. Lineberger, J. Phys. Chem. Ref. Data **14**, 731 (1985).
[38] K. A. Hanold, C. R. Sherwood, M. C. Garner, and R. E. Continetti, Rev. Sci. Instrum. **66**, 5507 (1995).
[39] K. A. Hanold, M. C. Garner, and R. E. Continetti, Phys. Rev. Lett. **77**, 3335 (1996).
[40] C. R. Sherwood, K. A. Hanold, M. C. Garner, K. M. Strong, and R. E. Continetti, J. Chem. Phys. **105**, 10803 (1996).
[41] O. H. W. Siegmund, K. Coburn, and R. F. Malina, IEEE Trans. Nucl. Sci. **32**, 443 (1985).
[42] C. Martin, P. Jelinsky, M. Lampton, R. F. Malina, and H. O. Anger, Rev. Sci. Instrum. **52**, 1067 (1981).
[43] O. H. W. Siegmund, R. F. Malina, K. Coburn, and D. Werthimer, IEEE Trans. Nucl. Sci. **NS-31**, 776 (1984).
[44] D. A. Dahl, J. E. Delmore, and A. D. Appelhans, Rev. Sci. Instrum. **61**, 607 (1990).
[45] Siegmund Scientific, 15 Sequoia Lane, Walnut Creek, CA 94595.
[46] M. J. Travers, D. C. Cowles, and G. B. Ellison, Chem. Phys. Lett. **164**, 449 (1989).
[47] K. A. Hanold, A. K. Luong, and R. E. Continetti, J. Chem. Phys. **109**, 9215 (1998).
[48] M. Lavollee and H. Bergeron, J. Phys. B **25**, 3101 (1992).
[49] R. T. Pack, R. B. Walker, and B. Kendrick, J. Chem. Phys. **109**, 6701 (1998).